Proceedings of the ASME 2024
International Design Engineering Technical Conferences and
Computers and Information in Engineering Conference
IDETC-CIE2024
August 25-28, 2024, Washington, DC

DETC2024-146396

ANALYTICAL INVESTIGATION OF ELECTROMECHANICALLY COUPLED HIERARCHICAL METAMATERIALS FOR SIMULTANEOUS VIBRATION ATTENUATION AND ENERGY HARVESTING

Ashenafi Mebrat, Joshua LeGrande, Oumar Barry*
Department of Mechanical Engineering
Virginia Polytechnic Institute and State University
Blacksburg, Virginia 24061

ABSTRACT

Recent work has revealed the great value of electromechanical resonators for energy harvesting and bandgap tuning in metamaterials. However, thus far there have not been any studies of hierarchically configured resonators for energy harvesting. This work presents a theoretical study of electromechanically coupled resonator-based hierarchical metamaterials, focusing on zero-order, first-order outward, and first-order inward configurations. The study investigates the impact of integrating resistor shunt circuits on the band structure under weak and strong coupling conditions. Additionally, it explores the influence of variations in local resonator mass on the vibration attenuation and energy harvesting capability of the configurations. The dispersion relations are determined for each configuration with varying system parameters. Furthermore, the transmissibility frequency response functions are presented to observe vibration reduction and energy harvesting capability. The results reveal that a hierarchical design offers enhanced flexibility in tailoring the band structure and stronger vibration attenuation and energy harvesting. As the hierarchy level increases, there is a corresponding increase in the number of passbands. However, it's noteworthy that weak electromechanical coupling does not influence the band structure across all hierarchy levels, while strong coupling does. Compared to the zero-order configuration's baseline performance, both the outward and inward configurations exhibit superior abilities in vibration suppression and energy harvesting when the total system mass is constant. Results given here may be used for the optimal design of hierarchically configured energy harvesters.

1 INTRODUCTION

Periodic structures are renowned for their wave-filtering properties within a specific frequency range called the band gap. Elastic wave dispersion of periodic structures has been extensively studied over an extended period [1]. In elastic periodic structures, Bragg scattering and local resonance are two primary bandgap formation mechanisms [2]. Metamaterials are periodic structures crafted from artificially designed atoms arranged either in patterns or randomly distributed manners [3]. Atoms of metamaterials are larger than typical atoms yet much smaller than the wavelengths of the waves they interact with. Wave dispersion properties of metamaterials are dictated by the configuration and properties of their respective meta-atoms.

Due to the challenges posed by the Bragg condition for achieving low-frequency bandgaps in small-sized metamaterials, the locally resonant mechanism was proposed by Liu et al. [4]. Coupling of metamaterials with local resonators finds applications in vibration control [2, 5], energy harvesting [6], structural protection [7], sound manipulation [8], and tunable devices [9, 10]. Locally resonant metamaterials can effectively attenuate vibrations by designing band gaps that align with the target frequencies, enabling selective rejection or attenuation of fre-

*Corresponding Author (Email: obarry@vt.edu)

quencies. Multiple numbers of local resonators, such as multiple periodic arrays of resonators on beams [1, 11], or multiple concentric mass-in-mass resonators [12, 13] can achieve broad and multi-low frequency bandgaps in elastic metamaterial beams.

Locally resonant metamaterials surpass Bragg-type phononic crystals by offering lower frequency stopbands in the same lattice volume, while also achieving comparable stopband frequencies with smaller unit cell dimensions [14]. In metamaterials, to achieve broad, multiple, and low frequency bandgap the techniques of multiple local resonators are employed [15–19]. The integration of localized resonators has emerged as a significant advancement in the manipulation of bandgap properties within the context of one-dimensional elastic wave propagation. Tailored band structures, achieved through the deployment of localized resonator mechanisms, hold immense appeal for various engineering applications. Numerous approaches have been proposed to customize the wave propagation behavior in one-dimensional mass-spring chain metamaterials [20–23].

Local resonators and negative capacitance piezoelectric (PZT) shunting methods are used to control the band structure in one-dimensional metamaterials [24]. The predominant approach for controlling the band gap in metamaterials involves integrating multiple, gradient, graded, or shunted piezoelectric local resonators on the mass-spring chain [25–29]. The band structure of an active elastic metamaterial incorporating a piezoelectric shunt can be actively controlled and tuned by adjusting the negative capacitance constant of the piezoelectric resonator. Piezoelectric-embedded local resonators have been investigated for vibration control applications in both active and passive periodic structures [24, 30, 31]. The use of a piezoelectric patch shunted with negative capacitance circuits for multimode damping of a beam structure has been demonstrated, showing its efficacy for vibration attenuation [32, 33]. Moreover, experimental research has shown that the elasticity of piezoelectric materials shunted with negative capacitance circuits can be electrically tuned [34].

Recent studies have investigated the impact of coupling electromechanical resonators on metamaterial-wave interactions [35, 36]. These studies found that weakly coupled electromechanical resonators with shunted circuits minimally alter wave dispersion, resulting in slight reductions in attenuation within the bandgap while allowing for simultaneous energy harvesting without affecting vibration control. Notably, strong electromechanical coupling can deform band structures, potentially merging acoustic and optical modes. Malla et al. further explored this by analyzing nonlinear electromechanical metamaterials with resistor and inductor shunts [37]. A triple passband structure was observed in strongly coupled electromechanical metamaterials featuring a single resonator coupled with resistors and inductors. In one-dimensional mass-spring chain metamaterial research, diverse design strategies aim to tailor band structures. Theoretical studies suggest hierarchical one-dimensional mass spring chain metamaterial designs as promising solutions to control elastic wave propagation [12, 15, 21, 25, 38].

So far, hierarchical and graded resonators without piezoelectric shunted circuits have been explored for elastic wave propagation offering versatile band structures. Even though recent work has focused on utilizing metamaterials for vibration control and energy harvesting with electromechanical elements like piezoelectric patches, there has been no study yet on hierarchical mass-spring metamaterials integrated with piezoelectric shunt circuits. In this study one-dimensional outward and inward hierarchical configurations of mass-spring chain metamaterials are considered. Analytical methods are employed to investigate the band structure with piezoelectric element integrated to local resonators shunted with resistor circuits. The general governing equations are derived, and the dispersion relations and displacement and voltage transmissibility are presented for both configurations. The dispersion relations of the hierarchical configurations are compared with the single resonator chain for the same total mass. Furthermore, the possible application of inward and outward configuration for simultaneous vibration reduction and energy harvesting is highlighted.

2 MODELING AND SOLUTION METHODS

A schematic diagram in Fig. 1 illustrates outward and inward hierarchical configurations of the system. In this setup, a unit cell consists of N piezoelectric embedded local resonators, each with masses denoted as $m_1, m_2, ..., m_N$, arranged within the outer mass m_0. Each outer mass is then coupled to another by a spring with stiffness, k_0, to form a 1D electromechanically coupled hierarchical metamaterial. The outward configuration (Fig. 1(a)) arranges the resonators in parallel while the inward configuration (Fig. 1(b)) arranges them in a nested series such that the n^{th} resonator is coupled to the n-1^{th} and n+1^{th} resonators. Unit cells are separated by a lattice distance, L, and each resonator is connected to a shunt circuit with load resistance, R. The hierarchical order of the chain is determined by N-1.

The governing equations for the j^{th} unit cell of the outward configuration are expressed as

$$m_0\ddot{u}_0^{(j)} - k_0u_0^{(j-1)} + 2k_0u_0^{(j)} - k_0u_0^{(j+1)} + \sum_{n=1}^{N} m_n\ddot{u}_n^{(j)} = 0 \quad (1)$$

$$m_n\ddot{u}_n^{(j)} - k_nu_0^{(j)} + k_nu_n^{(j)} + \theta_nv_n^{(j)} = 0 \quad (2)$$

$$R_nC_n\dot{v}_n^{(j)} + v_n^{(j)} + R_n\theta_n\dot{u}_0^{(j)} - R_n\theta_n\dot{u}_n^{(j)} = 0 \quad (3)$$

Equations 1 and 2, define the displacement of the outer mass, $u_0^{(j)}$, and the displacement of the n^{th} local resonator, $u_n^{(j)}$, and

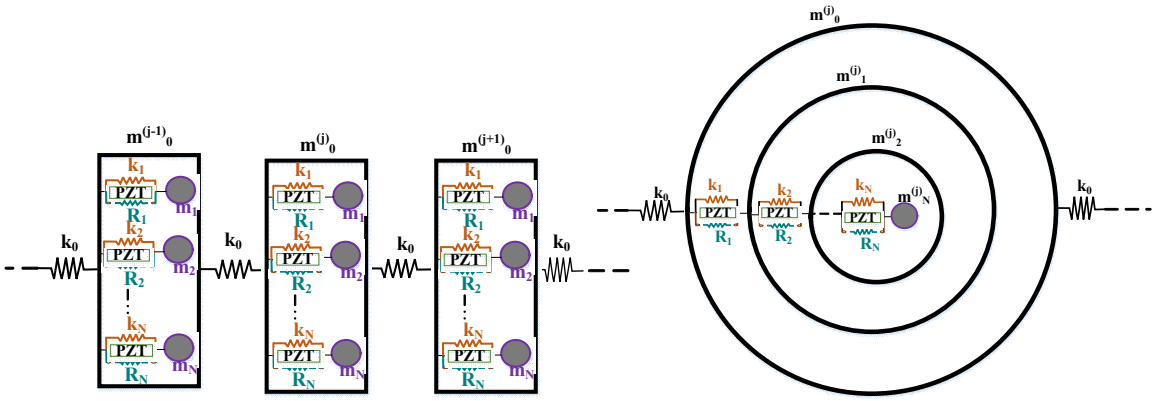

FIGURE 1: SCHEMATICS OF THE HIERARCHY: (a) OUTWARD AND (b) INWARD ELECTROMECHANICALLY COUPLED RESONATOR SHUNTED WITH PIEZOELECTRICAL MATERIAL (PZT) CONFIGURATION

equation 3 defines the voltage across the circuit shunted to the nth resonator, $v_n^{(j)}$. Here m_0 is the outer mass and m_n is mass of the nth local resonator. The stiffness of the outer spring and spring connecting the local resonators are k_0 and k_n, respectively. The nth piezoelectric element has an electromechanical coupling coefficient θ_n, capacitance C_n, and circuit load resistor R_n.

Similarly, for the inward configuration, the governing equations of motion are

$$m_0\ddot{u}_0^{(j)} - k_0u_0^{(j-1)} + (2k_0+k_1)u_0^{(j)} - k_0u_0^{(j+1)} - k_1u_1^{(j)} - \theta_1 v_1 = 0 \tag{4}$$

$$m_n\ddot{u}_n^{(j)} - k_nu_{n-1}^{(j)} + (k_n+k_{n+1})u_n^{(j)} - k_{n+1}u_{n+1}^{(j)} + \theta_n v_n^{(j)} - \theta_{n+1}v_{n+1}^{(j)} = 0 \tag{5}$$

$$R_nC_n\dot{v}_n^{(j)} + v_n^{(j)} + R_n\theta_n\dot{u}_{n-1}^{(j)} - R_n\theta_n\dot{u}_n^{(j)} = 0 \tag{6}$$

In equations 2, 3, 5, and 6, n ranges from 1 to N, determined by the configuration order. For instance, $N=1$ for zero-order and $N=2$ for first-order. We can assume general harmonic solutions of the form

$$\begin{aligned} u_0^{(j+m)} &= A_0e^{i((j+m)\kappa-\omega t)} \\ u_n^{(j)} &= A_ne^{i(j\kappa-\omega t)} \\ v_n^{(j)} &= B_ne^{i(j\kappa-\omega t)} \end{aligned}$$

to solve equations 1-6, where m is an integer $\ldots,-2,-1,0,1,2,\ldots$, t is time, ω is the angular frequency, and κ is the dimensionless wavenumber.

Substituting the presumed solution will yield a frequency wavenumber relationship used to determine the dispersion relations for these systems. The outward configuration yields

$$\left(2k_0\left(1-\cos\left(\kappa\right)\right) - m_0\omega^2\right)A_0 - \sum_{n=1}^{N} A_nm_n\omega^2 = 0 \tag{7}$$

$$-k_nA_0 + \left(k_n - m_n\omega^2\right)A_n + \theta_nB_n = 0 \tag{8}$$

$$-i\omega R_n\theta_nA_0 + i\omega R_n\theta_nA_n + \left(1-i\omega R_nC_n\right)B_n = 0 \tag{9}$$

while the inward configuration yields

$$\left(2k_0(1-\cos\left(\kappa\right)) - m_0\omega^2 + k_1\right)A_0 - k_1A_1 - \theta_1B_1 = 0 \tag{10}$$

$$-k_nA_{n-1} + \left(k_n+k_{n+1}-m_n\omega^2\right)A_n - k_{n+1}A_{n+1} + \theta_nB_n - \theta_{n+1}B_{n+1} = 0 \tag{11}$$

$$-i\omega R_n\theta_nA_{n-1} + i\omega R_n\theta_nA_n + \left(1-i\omega R_nC_n\right)B_n = 0 \tag{12}$$

TABLE 1: MATERIAL PARAMETERS USED IN THE ANALYSIS.

Parameter	m_0	ω_0, ω_1, ω_2	C_1, C_2	θ_1, θ_2 (Weak)	θ_1, θ_2 (Strong)
Value	0.125 kg	2×10^5 rad/s	1.13×10^{-10} F	1×10^{-10} N/V	0.3 N/V

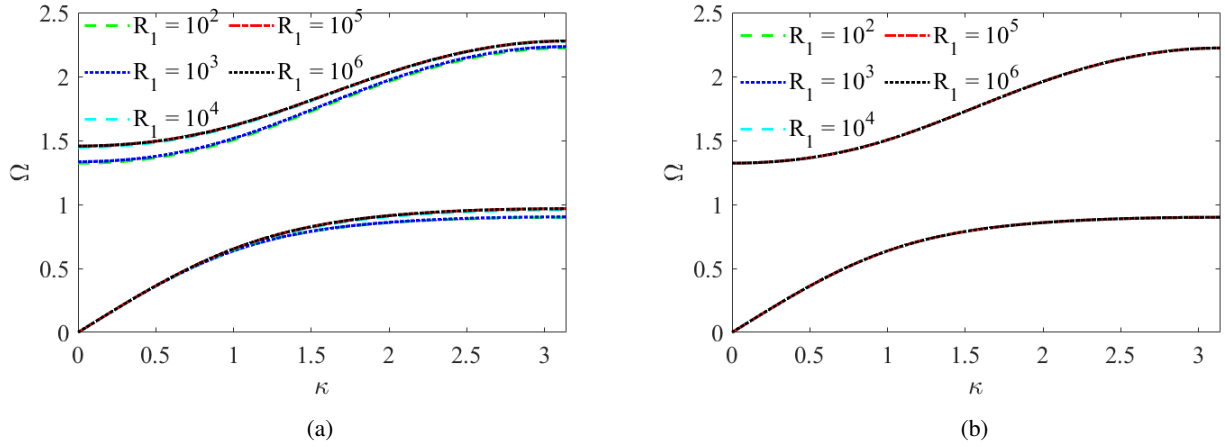

FIGURE 2: ZERO-ORDER DISPERSION AT DIFFERENT SHUNT CIRCUIT RESISTOR LOAD FOR (a) STRONG AND (b) WEAK COUPLING AT $\eta = 0.75$

3 WAVE DISPERSION

In this study, we will consider the zero-order (single resonator) case and the first-order (two resonators) case for both inward and outward configurations. The ratio of the total resonators mass to the outer mass is defined as $\eta = m_r/m_0$ where m_r is the total resonator mass. The ratio of the n^{th} resonator to the total mass of the resonators is $\beta_n = m_n/m_r$. The normalized frequency is defined as $\Omega = \omega/\omega_0$, where $\omega_0 = \sqrt{k_0/m_0}$. The parameters used for analysis are adopted from reference [37] and summarized in Table 1.

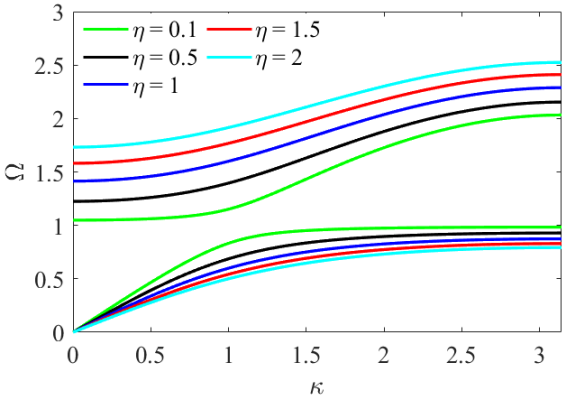

FIGURE 3: THE EFFECT OF MASS RATIO, η, ON WEAKLY COUPLED ZERO-ORDER HIERARCHY

3.1 Zero-order Configuration

The zero-order hierarchy configuration has a single electromechanical resonator, and the configuration is the same for outward and inward systems. Figure 2 displays the wave dispersion characteristics of an electromechanically coupled zero-order hierarchical metamaterial for weak and strong coupling with varying values for the shunt circuit resistor. Notably, the resistor demonstrates an effect in strong coupling but exhibits negligible influence in weak coupling scenarios. In cases of strong coupling, the resistor's effect becomes pronounced, particularly towards the lower bound of the second passband. The band structure is significantly affected between 10^3 and 10^4 Ω and shows a broad band gap. These results agree well with previous work [35]. Similar results obtained at other values of the mass ratio, η, reveal these trends to be valid regardless of mass ratio.

The graph in Fig. 3, illustrates the influence of the resonator mass ratio, η , on the wave dispersion phenomena of weakly coupled zero-order hierarchy with a shunt circuit resistance of $10^4\Omega$. Unless otherwise explicitly stated, all the effects of the resonator mass ratio are examined with a shunt circuit resistor $10^4\Omega$. Since strongly coupled systems lack engineering applications [39], the effect of mass ratio is exclusively examined here within weakly coupled systems. The width of the band gap is proportional to the value of η, with the band gap width increasing as η increases.

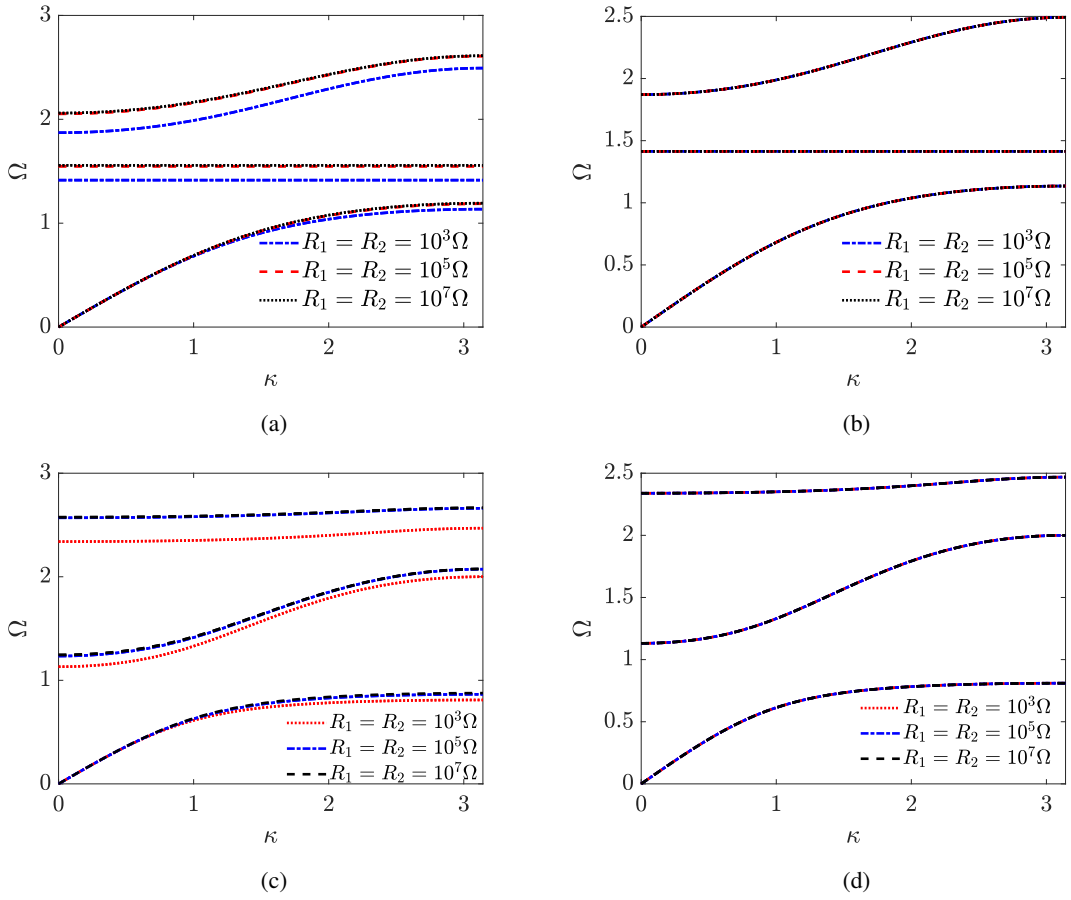

FIGURE 4: THE EFFECTS OF SHUNT CIRCUIT RESISTORS ARE INVESTIGATED ACROSS VARIOUS CONFIGURATIONS: (a) STRONGLY COUPLED OUTWARD CONFIGURATION, (b) WEAKLY COUPLED OUTWARD CONFIGURATION, (c) STRONGLY INWARD CONFIGURATION, AND (d) WEAKLY COUPLED INWARD CONFIGURATION AT $\beta_1 = 0.5$

3.2 First-order Configuration

The first-order hierarchy contains two electromechanical resonators. The resonator mass and stiffness parameters are $m_1 = \eta\beta_1 m_0$, $m_2 = \eta(1-\beta_1)m_0$, and $k_1 = k_2 = 4e^{10}m_r$. The electromechanical parameters remain the same as before. For this analysis, the total resonator mass is kept constant. More emphasis is instead given to the effect of resonator masses relative to one another through β_1.

The wave dispersion of the first-order configuration at $\beta_1 = 0.5$ is given in Fig. 4 for both inward and outward configurations. These demonstrate the effects of different shunt circuit resistor values on the band structures. The plots show the relationship between normalized frequency and normalized wave number, where the influence of the shunt circuit resistor appears to be analogous to that observed in the zero-order configuration. The variation of the shunt circuit resistor has a noticeable impact in the case of strong coupling, as evidenced in Figs. 4 (a) and (c), whereas it exhibits no significant effect on the band structures for the weakly coupled system, as shown in Figs. 4 (b) and (d). This highlights how the coupling strength can dictate the sensitivity of the system's band structure to changes in the shunt resistor values.

Strong coupling substantially impacts the second and third passbands for both the outward and inward configurations. While the effect on the first passband at low frequencies is almost negligible, there is a pronounced influence on the first passband during high-frequency propagation. The variation in the shunt circuit resistor does not significantly affect the band structure in a weakly coupled electromechanical system.

3.3 Effect of Resonator Mass Ratios

This section delves into the impact of the resonator mass ratios β_1 and η on the band structure for both first-order outward and inward configurations. The effect of β_1 can be seen in Fig. 5(a) and (c), and the effect of η is shown in Fig. 5(b) and (d). To isolate individual effects, η is kept constant at $\eta = 0.75$ when β_1 is varied, and β_1 is kept constant at $\beta_1 = 0.85$ when η is varied.

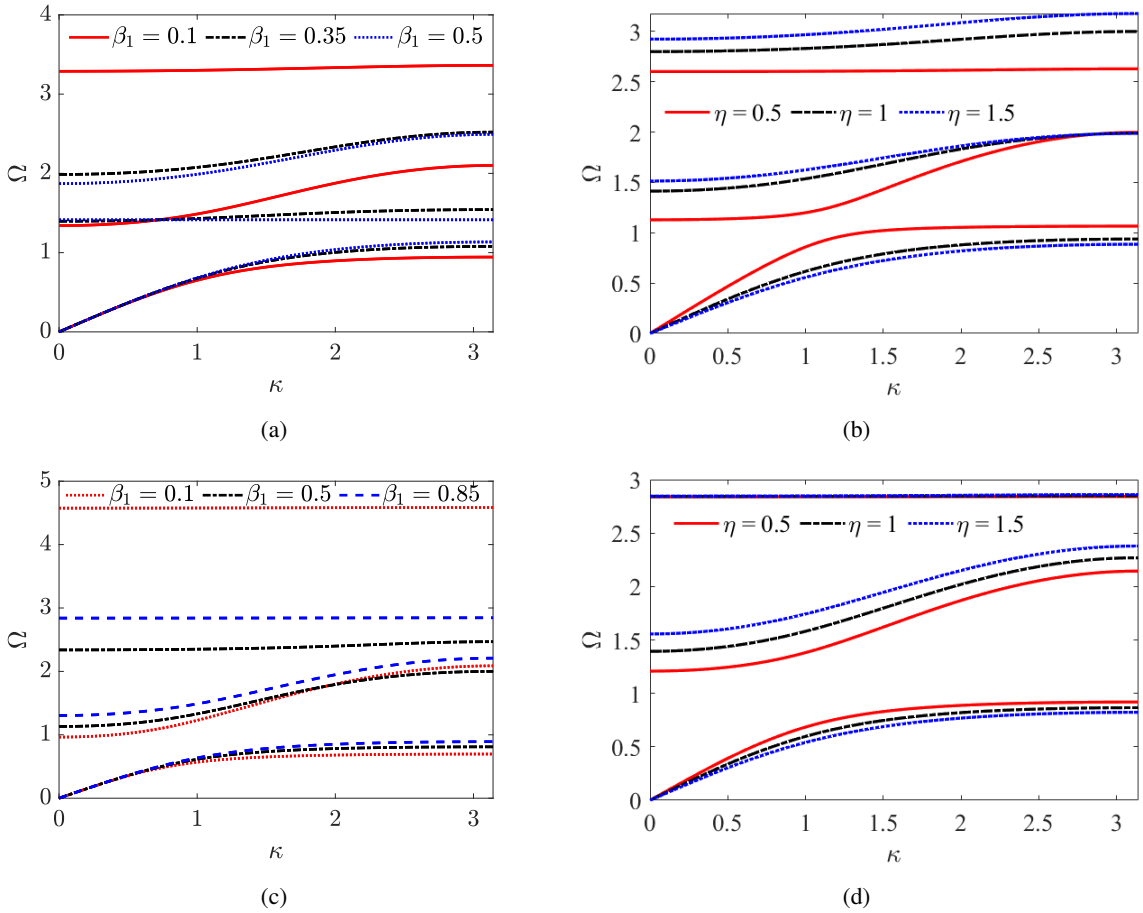

FIGURE 5: FIRST-ORDER WEAKLY COUPLED DISPERSION OBSERVED AT DIFFERENT MASS RATIOS (β_1 AND η) IN (a) AND (b) FOR OUTWARD CONFIGURATION, AND IN (c) AND (d) FOR INWARD CONFIGURATION

For both inward and outward configurations, the resonator mass has a considerable influence on the band structure. Decreasing the first resonator mass ratio, β_1, to a smaller value affects the third passband frequency magnitude and shape. At a reduced value of β_1 , this passband tends to appear as an almost flat band, propagating at elevated frequencies, as illustrated in Fig. 5 (a) and (c) with $\beta_1 = 0.1$. On the other hand, increasing the value of β_1 up to $\beta_1 = 0.5$ reduces the width of the second band gap for both configurations and the width of the first bandgap for the outward configuration.

As shown in Fig. 5, for normalized frequencies below 0.5, the first passband is not strongly affected by variations in β_1 in either configuration. However, the upper limit of the first passband frequency increases with the resonator mass ratio up to 0.5.

For the outward configuration, the trends in the band structure are symmetric about β_1=0.5 since, in this configuration, the distinction between m_1 and m_2 is arbitrary. When $\beta_1 = 0.5$, the resonators have the same mass, and the second passband of the outward configuration becomes flat with zero width. In addition, this passband is independent of η. However as β_1 approaches 0 or 1, the second passband regains its shape, increasing in width, and the third passband becomes flatter and moves to a higher frequency.

In the case of the inward configuration, this symmetry is not present. As β_1 approaches and exceeds 0.5, the upper limit of the first passband continues to increase. When β_1 approaches 0.5 from below, the second passband becomes narrower. When the value of β_1 exceeds 0.5, the second passband stops shrinking but shifts upward in frequency. The third passband is at its lowest frequency range when $\beta_1 = 0.5$, with increasing frequency for higher or lower values of β_1. However, this is not symmetric, and values less than 0.5 produce a higher frequency range for the third band than values above 0.5.

With the total mass of the resonator being constant, the bandgap width for the zero-order system remains narrow compared to either first-order system. For the outward configuration, the total bandgap width decreases as β_1 approaches 0.5. At $\beta_1 = 0.5$ however, if the second passband with zero width

is neglected, then the outward configuration produces a single ultra-wide bandgap. It will be shown in the next section that this assumption is valid. For the inward configuration, the first band gap increases with β_1 with a maximum width at $\beta_1 = 1$. The second band gap however is maximized at very low β_1 values. In general, the outward configuration provides slightly wider total band gap width than the inward configuration except for at very low values of β_1. However, for $\beta_1 > 0.5$, the inward configuration produces wider low-frequency bandgaps.

The first-order hierarchical system responds very sensitively to changes in η. For both outward and inward first-order designs, increasing η leads to a wider overall bandgap (Figure 5(b) and (d)). The third passband frequency magnitude in the outward configuration (Figure 5(b)) increases with η, resulting in a broad second bandgap. The passband frequency range increases as well. However, at a lower value of β_1 increasing the value of η beyond 1, the third passband diminishes in width but still propagates at raised frequency. At higher values of β_1 (above 0.85), the first and second passband of outward configuration reveals a similar dispersion nature as the zero-order system. Thus, at a larger value of η the outward configuration provides a broad first bandgap. It is again interesting to note that for the outward configuration, at $\beta_1 = 0.5$, the flat second passband remains fixed and is independent of variations in η.

The first and second passbands of the inward configuration, depicted in Figure 5(d), demonstrate an identical reaction to the zero-order configuration for disparity of η. As the value of η moves further away from 1, the width of the second passband will become very small if β_1 is greater than 0.5. For a higher η value its width increases if β_1 is becoming less than 0.5. The third passband propagates at a higher frequency as η increases. When β_1 is less than 0.5, the third passband width grows. On the other hand, when β_1 is larger than 0.5, its passband width decreases.

Irrespective of hierarchies, η has a compressing effect on the upper limits of the first passband as it increases. This effect increases width of the first bandgap.

4 TRANSMISSIBILITY

In this section, the strength of vibration attenuation and energy harvesting are determined for each configuration through the frequency response of the outermost cell displacement and voltage across each shunt circuit. The transmissibility determination is based on comparing the amplitude of outer mass displacement to the amplitude of excitation force in the weakly coupled system using the transfer function method.

The outer mass displacement transmissibility of a unit cell is shown in Fig. 6 as a function of normalized frequency for each configuration with multiple β_1 values. The zero-order configuration features two peaks and one valley. However, owing to the hierarchical structure, the first-order configurations exhibit three peaks and two valleys. For $\beta_1 = 0.15$, shown in Fig. 6(a), both the inward and outward configurations have a narrower first bandgap than the zero-order configuration with comparable attenuation levels. However, they both surpass the zero-order configuration in their second bandgap range with the outward configuration yielding the strongest attenuation in this range. The inward configuration maintains its behavior when $\beta_1 = 0.5$ (Fig. 6(b)), maintaining a narrower and shallower first bandgap than the zero-order configuration but showing stronger attenuation in the range of its second bandgap. At this point, the outward configuration hosts a single band gap that is significantly wider and deeper than both of the other cases. The outward configuration at $\beta_1 = 0.5$ contains two peaks. Because the electromechanical resonators have equal masses, the two peaks triggered by local electromechanical resonators come together. As β_1 increases to $\beta_1 = 0.85$, shown in Fig. 6(c), all three configurations become very comparable within the range of the first bandgap. Beyond the second resonant peak, only the outward configuration shows significant vibration attenuation. In general, the outward configuration tends to provide the strongest vibration attenuation of the three configurations with the lowest displacement transmissibility. Meanwhile, the inward configuration does not show much improvement over the zero-order configuration except for at higher frequencies.

The voltage transmissibilities of the circuits shunted to the first and second resonators are plotted in Fig. 7 at $\beta_1 = 0.15$. Voltage harvested from the zero-order configuration displays two peaks without any considerable voltage output decline. However, for the first-order configuration, there are notable drops in voltage output at specific frequencies. Within the inward configuration in Fig. 7 (a), a voltage drop is noticeable only within the first circuit. Nonetheless, this drop extends across a broad frequency range, thereby substantially impacting the overall harvested energy. In contrast, the outward configuration demonstrates voltage drops in both the first and second circuits, albeit limited to a short frequency range for each circuit.

To better compare the total energy harvested by each configuration, Fig. 8 plots the voltage output from the zero-order configuration alongside the summed voltage output from both circuits in each first-order configuration. The total voltage transmissibility trend remains consistent for all β_1. Generally, the outward configuration demonstrates superior voltage output compared to both the zero-order and inward configurations across a wide range of frequency spectrum, as shown in Fig. 8 (a)-(c). For $\beta_1 = 0.5$, the total voltage transmissibility, as depicted in Fig. 8 (b), show off two peaks with relatively higher peak values.

However, when analyzing the total voltage transmissibility curves within specific frequency ranges, it becomes apparent that the inward configuration produces a higher voltage than the outward configuration, as evidenced by the pink-colored circles in Fig. 8 (a). When the value of β_1 reaches 0.45 shown in Fig. 8 (c), the inward configuration demonstrates a notably superior

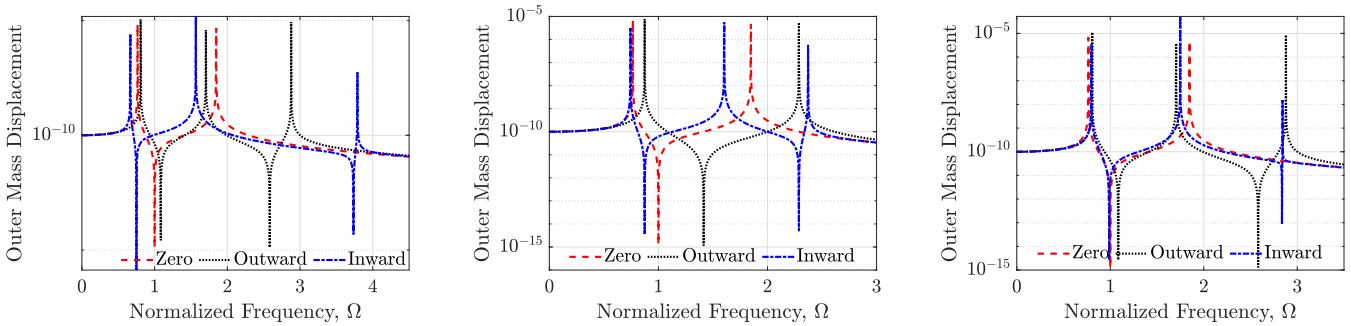

FIGURE 6: DISPLACEMENT TRANSMISSIBILITY OF OUTER MASS AT $\eta = 0.75$ AND (a) $\beta_1 = 0.15$, (b) $\beta_1 = 0.5$, AND (c) $\beta_1 = 0.85$.

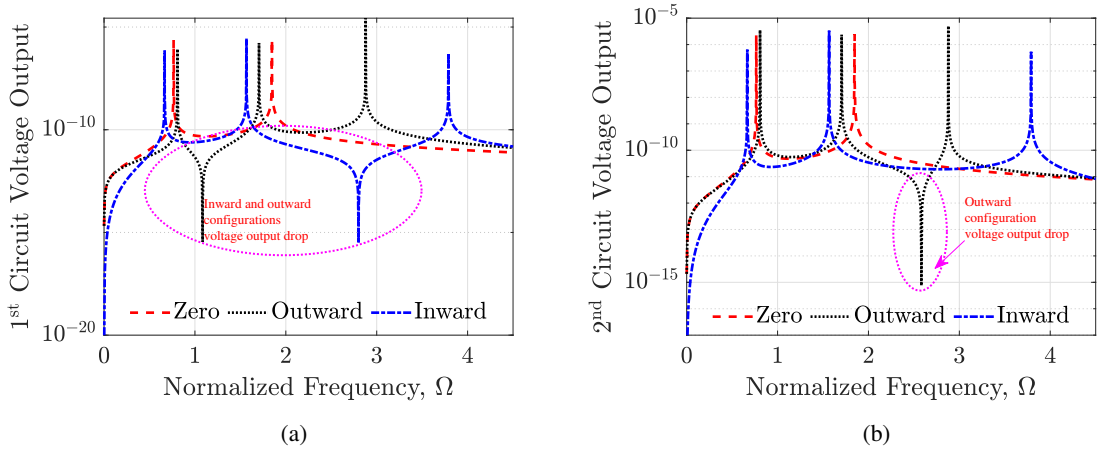

FIGURE 7: HARVESTED VOLTAGE TRANSMISSIBILITY OF (a) FIRST CIRCUIT AND (b) SECOND CIRCUIT AT $\eta = 0.75$ AND $\beta_1 = 0.15$.

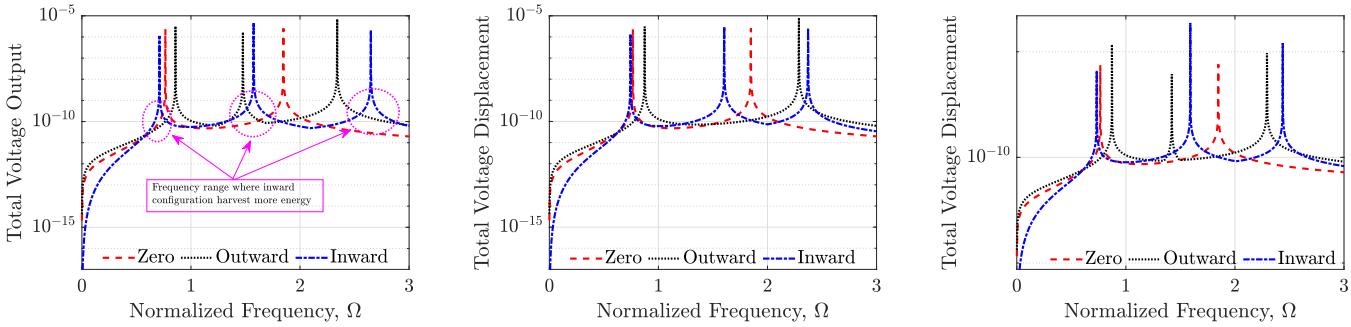

FIGURE 8: TOTAL VOLTAGE TRANSMISSIBILITY AT $\eta = 0.75$ AND (a) $\beta_1 = 0.35$, (b) $\beta_1 = 0.5$, AND (c) $\beta_1 = 0.45$

voltage output within a relatively broad range of normalized frequencies, spanning from 1.21 to 1.83. During this scenario, the inward configuration becomes capable of yielding a total peak voltage output of $2.29e^{-4}$ V/N.

Finally, the mean voltage output is examined to draw a comprehensive conclusion, as depicted in Fig. 9. This graph presents the relation of mean voltage output and β_1 for $\eta = 0.75$. Determination of the mean voltage output considers the system is operating over the entire passband frequency range from $0 \leq \Omega \leq 3$. Then the sum of first and second circuit voltage output is taken to get the total voltage output of the system. The mean voltage output was generated by averaging the total voltage output across

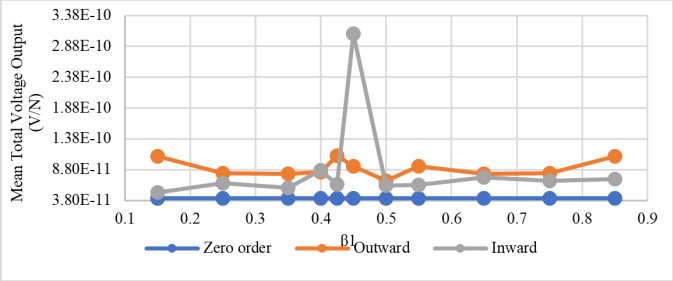

FIGURE 9: COMPARISON OF MEAN VOLTAGE OUTPUT TRANSMISSIBILITY BETWEEN ZERO AND FIRST-ORDER CONFIGURATIONS FOR THE SAME TOTAL MASS OF $1.75m_0$.

all data points. It illustrates, as shown in Fig. 9, the typical dominance of the outward configuration in harvesting energy over both the zero-order and inward configurations. However, this trend undergoes a reversal at the specific setup where the first resonator mass to the total mass ratio equals 0.45. Importantly, both configurations show improved energy harvesting over the traditional zero-order configuration.

5 CONCLUSION

This study explores the influence of incorporating shunt circuits on the band structure of hierarchical metamaterials and the effectiveness of these configurations for simultaneous vibration attenuation and energy harvesting. The band structures of electromechanically coupled zero-order, outward, and inward first-order hierarchies were examined for applications in vibration suppression and energy harvesting. The first-order hierarchy features three passbands, whereas the zero-order configuration has two passbands. Consequently, increasing the hierarchy enhances the number of passbands and band gaps, providing greater flexibility in adjusting the band structure through hierarchical design. Weak electromechanical coupling shows no impact on the dispersion relations for any configuration while stronger coupling produces a dependence on the circuit resistance.

When considering simultaneous vibration attenuation and energy harvesting, both hierarchical configurations demonstrate superior performance in both areas compared to the zero-order configuration with the same total mass. The hierarchical configurations display wider bandgaps and harvest more energy. In general, the outward configuration performs better than the inward configuration with deeper vibration attenuation and more energy harvested over wider frequency ranges. Although, the inward configuration is more versatile and can be designed to outperform the outward configuration at specific operation frequencies. Through proper design of either inward or outward configurations, more effective and lightweight energy harvesting is possible.

ACKNOWLEDGEMENTS

This work is supported in part by the National Science Foundation (NSF) Grant CMMI-2038187.

REFERENCES

[1] Xiao, Y., Wen, J., and Wen, X., 2012. "Broadband locally resonant beams containing multiple periodic arrays of attached resonators". *Physics Letters A,* ***376***(16), pp. 1384–1390.

[2] Lin, S., Zhang, Y., Liang, Y., Liu, Y., Liu, C., and Yang, Z., 2021. "Bandgap characteristics and wave attenuation of metamaterials based on negative-stiffness dynamic vibration absorbers". *Journal of Sound and Vibration,* ***502***, p. 116088.

[3] Lee, D., Nguyen, D. M., and Rho, J., 2017. "Acoustic wave science realized by metamaterials". *Nano convergence,* ***4***, pp. 1–15.

[4] Liu, Z., Zhang, X., Mao, Y., Zhu, Y., Yang, Z., Chan, C. T., and Sheng, P., 2000. "Locally resonant sonic materials". *Science,* ***289***(5485), pp. 1734–1736.

[5] Hu, G., Tang, L., Das, R., Gao, S., and Liu, H., 2017. "Acoustic metamaterials with coupled local resonators for broadband vibration suppression". *AIP Advances,* ***7***(2).

[6] Dwivedi, A., Banerjee, A., Adhikari, S., and Bhattacharya, B., 2021. "Optimal electromechanical bandgaps in piezo-embedded mechanical metamaterials". *International Journal of Mechanics and Materials in Design,* ***17***(2), pp. 419–439.

[7] Contreras, N., Zhang, X., Hao, H., and Hernández, F., 2023. "Application of elastic metamaterials/meta-structures in civil engineering: A review". *Composite Structures*, p. 117663.

[8] Fang, X., Wen, J., Bonello, B., Yin, J., and Yu, D., 2017. "Ultra-low and ultra-broad-band nonlinear acoustic metamaterials". *Nature communications,* ***8***(1), p. 1288.

[9] Bukhari, M., and Barry, O., 2023. "Broadband electromechanical diode: acoustic non-reciprocity in weakly nonlinear metamaterials with electromechanical resonators". *Journal of Vibration and Acoustics,* ***145***(2), p. 021003.

[10] Zhou, W., Li, X., Wang, Y., Chen, W., and Huang, G., 2018. "Spectro-spatial analysis of wave packet propagation in nonlinear acoustic metamaterials". *Journal of Sound and Vibration,* ***413***, pp. 250–269.

[11] Zhou, J., Wang, K., Xu, D., and Ouyang, H., 2017. "Multi-low-frequency flexural wave attenuation in euler–bernoulli beams using local resonators containing negative-stiffness mechanisms". *Physics Letters A,* ***381***(37), pp. 3141–3148.

[12] Zhao, J., Zhou, H., Yi, K., Kovacic, I., and Zhu, R., 2023. "Ultra-broad bandgap induced by hybrid hardening and softening nonlinearity in metastructure". *Nonlinear Dynamics,* ***111***(19), pp. 17687–17707.

[13] Gao, C., Halim, D., and Yi, X., 2022. "Elastic metamaterial with multiple resonant modes and asymmetric structure design for low-frequency vibration absorption". *Acta Mechanica,* ***233***(12), pp. 5321–5333.

[14] Elmadih, W., Chronopoulos, D., Syam, W., Maskery, I., Meng, H., and Leach, R., 2019. "Three-dimensional resonating metamaterials for low-frequency vibration attenuation". *Scientific reports,* ***9***(1), p. 11503.

[15] Zhao, P., Zhang, K., Zhao, C., and Deng, Z., 2021. "Multi-resonator coupled metamaterials for broadband vibration suppression". *Applied Mathematics and Mechanics,* ***42***(1), pp. 53–64.

[16] Gao, Y., Wang, L., Sun, W., Wu, K., and Hu, H., 2022. "Ultrawide bandgap in metamaterials via coupling of locally resonant and bragg bandgaps". *Acta Mechanica,* ***233***(2), pp. 477–493.

[17] Gorshkov, V., Sareh, P., Navadeh, N., Tereshchuk, V., and Fallah, A. S., 2021. "Multi-resonator metamaterials as multi-band metastructures". *Materials & Design,* ***202***, p. 109522.

[18] Li, Q., He, Z., Li, E., and Cheng, A., 2019. "Design of a multi-resonator metamaterial for mitigating impact force". *Journal of Applied Physics,* ***125***(3).

[19] Huang, G., and Sun, C., 2010. "Band gaps in a multiresonator acoustic metamaterial". *Journal of Vibration and Acoustics,* ***132***(3), p. 031003.

[20] Hu, G., Tang, L., Xu, J., Lan, C., and Das, R., 2019. "Metamaterial with local resonators coupled by negative stiffness springs for enhanced vibration suppression". *Journal of Applied Mechanics,* ***86***(8), p. 081009.

[21] Xu, X., Barnhart, M. V., Li, X., Chen, Y., and Huang, G., 2019. "Tailoring vibration suppression bands with hierarchical metamaterials containing local resonators". *Journal of Sound and Vibration,* ***442***, pp. 237–248.

[22] Dwivedi, A., Banerjee, A., and Bhattacharya, B., 2020. "Dynamics of piezo-embedded negative stiffness mechanical metamaterials: A study on electromechanical bandgaps". In ASME International Mechanical Engineering Congress and Exposition, Vol. 84478, American Society of Mechanical Engineers, p. V001T01A015.

[23] Bukhari, M., and Barry, O., 2022. "Substantial frequency conversion at long-wavelength limit in metamaterial with weakly nonlinear local electromechanical resonators: Analytical, computational, and experimental study". *International Journal of Non-Linear Mechanics,* ***147***, p. 104226.

[24] Chen, Y., Huang, G., and Sun, C., 2014. "Band gap control in an active elastic metamaterial with negative capacitance piezoelectric shunting". *Journal of Vibration and Acoustics,* ***136***(6), p. 061008.

[25] Liang, X., Zhang, F., and Jiang, J., 2022. "Ultra-wideband outward-hierarchical metamaterials with graded design". *International Journal of Mechanics and Materials in Design,* ***18***(1), pp. 169–184.

[26] Zhao, B., Thomsen, H. R., De Ponti, J. M., Riva, E., Van Damme, B., Bergamini, A., Chatzi, E., and Colombi, A., 2022. "A graded metamaterial for broadband and high-capability piezoelectric energy harvesting". *Energy Conversion and Management,* ***269***, p. 116056.

[27] Zhang, J., Qian, D.-h., Ren, L., and Wang, Q., 2023. "Electro-mechanical coupling properties of band gaps in an elastic/piezoelectric phononic crystal nonlocal nanobeam with periodically attached "spring-mass" resonators". *Applied Mathematics-A Journal of Chinese Universities,* ***38***(3), pp. 429–443.

[28] Xu, J., Lu, H., Qin, W., Wang, P., and Bian, J., 2022. "Mechanical shunt resonators-based piezoelectric metamaterial for elastic wave attenuation". *Materials,* ***15***(3), p. 891.

[29] Yi, K., Liu, Z., and Zhu, R., 2021. "Multi-resonant metamaterials based on self-sensing piezoelectric patches and digital circuits for broadband isolation of elastic wave transmission". *Smart Materials and Structures,* ***31***(1), p. 015042.

[30] Tang, J., and Wang, K., 1999. "Vibration control of rotationally periodic structures using passive piezoelectric shunt networks and active compensation".

[31] Tang, J., and Wang, K.-W., 2001. "Active-passive hybrid piezoelectric networks for vibration control: comparisons and improvement". *Smart Materials and Structures,* ***10***(4), p. 794.

[32] Behrens, S., Fleming, A., and Moheimani, S., 2003. "A broadband controller for shunt piezoelectric damping of structural vibration". *Smart materials and structures,* ***12***(1), p. 18.

[33] Park, C. H., and Park, H. C., 2003. "Multiple-mode structural vibration control using negative capacitive shunt damping". *KSME international journal,* ***17***, pp. 1650–1658.

[34] Imoto, K., Nishiura, M., Yamamoto, K., Date, M., Fukada, E., and Tajitsu, Y., 2005. "Elasticity control of piezoelectric lead zirconate titanate (pzt) materials using negative-capacitance circuits". *Japanese journal of applied physics,* ***44***(9S), p. 7019.

[35] Bukhari, M. A., Qian, F., Barry, O. R., and Zuo, L., 2020. "Effect of electromechanical coupling on locally resonant metastructures for simultaneous energy harvesting and vibration attenuation applications". In Dynamic Systems and Control Conference, Vol. 84287, American Society of Mechanical Engineers, p. V002T38A003.

[36] LeGrande, J., Bukhari, M., and Barry, O., 2023. "Effect of electromechanical coupling on locally resonant quasiperiodic metamaterials". *AIP Advances,* ***13***(1), p. 015112.

[37] Malla, A., Bukhari, M., and Barry, O., 2022. "Modeling and analysis of a nonlinear locally resonant metamaterial with inductance shunt". In *Earth and Space 2022*. pp. 504–

515.
[38] Liu, C., and Reina, C., 2018. “Broadband locally resonant metamaterials with graded hierarchical architecture”. *Journal of Applied Physics,* ***123***(9).
[39] Erturk, A., and Inman, D. J., 2011. *Piezoelectric Energy Harvesting*. John Wiley & Sons.